This paper can be found at https://doi.org/10.1016/j.conbuildmat.2021.125228

AN ANALYTICAL BOND STRESS-SLIP MODEL FOR A TRM COMPOSITE COMPATIBLE WITH RAMMED EARTH

Romanazzi A.[a], Oliveira D.V.[b] and Silva R.A.[c]

[a] University of Minho, ISISE, Department of Civil Engineering, Guimarães, Portugal, aromanazzi89@gmail.com

[b] University of Minho, ISISE, Department of Civil Engineering, Guimarães, Portugal, danvco@civil.uminho.pt

[c] University of Minho, ISISE, Department of Civil Engineering, Guimarães, Portugal, ruisilva@civil.uminho.pt

ABSTRACT

A textile reinforced mortar (TRM) compatible with rammed earth structures is proposed to mitigate their seismic vulnerability. Being TRM a composite material, defining the matrix-fibre interface relationship is fundamental to predict the performance of strengthened structures. In this framework, an existing analytical approach with a newly damage model was adapted to a specific TRM composite system that is not yet addressed in literature. Hence, an adhesion-friction law was calibrated with basis on recent experimental observations. In conclusion, the proposed algorithm reproduces adequately the elastic and nonlinear response of the matrix-fibre interface and predicts with accuracy the pull-out strength of the composite.

Keywords: rammed earth, analytical model, bond stress-slip law, textile reinforced mortar, direct boundary approach

1. INTRODUCTION

Raw earth is one of the most ancient building materials and its related building techniques are spread worldwide. The importance of this building material stands out from the fact that 20% to 30% of the world population is estimated to live in earthen dwellings and that more than 10% of the built World Heritage classified by UNESCO is made of earth [1][2]. Among the different building techniques based on the use of raw earth, rammed earth consists in compacting a mixture of moistened earth within a formwork [1][3]. This technique has been used since ancient times to build from monuments [1][4][5] to affordable dwellings [6][7]. Nonetheless, earthen buildings are a subject of increasing concern as they present a high seismic vulnerability,

which is due to low mechanical properties of the material, high self-weight and poor connections between structural elements. Thus, moderate to intense earthquakes are expected to result in in-plane cracking of the walls, formation of out-of-plane mechanisms and potential collapse of the roof and floors [8][9].

Recently, textile reinforced mortar (TRM) composites have been proposed as an alternative strengthening solution because of the low self-weight, high tensile strength and ductility capacity, as already demonstrated for masonry buildings [10][11][12][13]. Some experimental studies on TRM-based strengthening systems for earthen buildings were conducted on adobe structural elements and mock-ups, which evidenced to be an efficient solution to reduce their seismic vulnerability [14][15][16][17][18][19][20][21].

Although the investigation on TRM strengthening for rammed earth structures is recent and the first outcomes show potential improvement of the overall seismic capacity [7][22][23], the research carried out so far overlooked the local response of the system in favour of investigating its global effect on full structures or structural components. In addition, insufficient attention is paid to the compatibility between the proposed strengthening solutions and rammed earth substrates, which guarantees the long-term effectiveness of the interventions [24]. Yet, in composite materials, the definition of the mechanical properties of the matrix-fibre interface, known as bond stress-slip relationship (BSR), is of primary importance to understand and predict the overall performance of a strengthened structure. In this context, different test setups have been implemented to describe the interaction between the two components of TRM and to deduce consistent interface models [25][26][27]. Pull-out tests are among these setups and consist of pulling out a single fibre or a mesh band embedded in a specimen representative of the matrix, while the corresponding load-displacement relationship $P(u)$ is recorded. However, the resistance to debonding depends on the mechanical and chemical properties of the matrix-mesh interface and the interfacial bond area, which is a function of the embedded length and fibre diameter. Therefore, the $P(u)$ relationship is a response of a system with a specific geometry, not representing a material property of the tested composite. For obtaining material parameters to define the shear force transmission independently from the geometric properties, numerical or analytical models can be applied to the experimental $P(u)$ curves [28][29].

In general, analytical interface models can be divided in two main groups [30]: a) perfect interface model, mainly used in the case of stress transfer problems of resin matrix composites (e.g. FRP) [31]; b) imperfect interface models, usually implemented in the case of cement-based matrix composites [30]. In the case of

imperfect bond (granted by cohesion and adhesion mechanisms), a transition zone (interface) is assumed with properties different from the matrix and fibre. Consequently, when the stiffness of the interface is much smaller than that of the adjacent constituents, the deformation in this zone can be higher than that of the fibre u_f or matrix u_m. Therefore, the difference between the deformation of the components represents the interface deformation and it is defined as slip [$s=u_f-u_m$] [32]. Hence, the bond stress-slip law represents the idealization of the shear stress $\tau(s)$ transfer at the interface matrix-fibre at any coordinate of the fibre x as a function of the slip s [30][32][33][34].

To infer the analytical law of the mortar-mesh interaction for imperfect interface models, mainly two approaches are used, namely considering a direct boundary problem (DBP) or an inverse boundary problem (IBP). For DBP, the load versus displacement relation $P(u)$ of a pull-out test is calculated on basis of an assumed constitutive law $\tau(s)$ [30][35][36][37][38]. To derive such a bond stress-slip relationship for a material combination, its parameters must be assumed to simulate the pull-out curve, whose outcome is compared with the experimental data. The bond-slip law is defined once the best approximation is achieved by means of fitting or other optimization processes. Nevertheless, the direct approach entails complex mathematical problems, since the simultaneous optimization of many parameters is difficult to perform. For this reason, only a limited number of free parameters are typically considered, meaning that the general mathematical description of the bond-slip might be restricted. Regarding the inverse boundary problem, the analytical solution is determined directly from a given experimental $P(u)$ curve [29][33][39]. Thus, the constitutive law is not restricted in number of parameters as in the case of the direct boundary problem. On the other hand, the constitutive law is stepwise defined with basis on the identification of the pair $[\tau\text{-}s]_{(i)}$ in an iterative algorithm, which in turn depends on the previously determined pair $[\tau\text{-}s]_{(i-1)}$, meaning that the error introduced by the adopted tolerance keeps accumulating with further steps. The growing of such inaccuracy since earlier derivation steps can result in oscillation effects or even in a diverging calculation, for which further regularization methods in the numerical solution routine are required.

Considering the existing approaches to infer the analytical law of the interaction mortar-mesh and the experimental results presented in Romanazzi *et al.* [40], the direct approach was adopted to infer a bond stress-slip relationship for the specific TRM composite system, not yet addressed in literature. This paper presents firstly the materials characterization and the results of pull-out tests from a previous experimental program

conducted by the authors, which allowed to hypothesize the BSR. Subsequently, the problem statement of the analytical model with the implementation of a novel damage model is derived. Afterwards, the algorithm for solving the problem and analytically simulate the pull-out test is proposed and discussed. Finally, a sensitivity analysis is performed, and the constitutive law verified for the specific composite material.

2. EXPERIMENTAL PROGRAM OVERVIEW

The material properties and the results of a previous series of pull-out tests conducted by the authors are here briefly reported for convenience, nonetheless further details can be found in Romanazzi *et al.* [40]. The referred experimental program proposed a TRM strengthening solution for rammed earth, composed of an earth-based mortar and a low-cost glass fibre mesh and compatible with the substrate from the physical and mechanical points of view [24]. The earth-based mortar was manufactured with soil sieved through a 2 mm aperture sieve and fine sand, in proportions that resulted in a clay content of 11% to mitigate cracking due to drying shrinkage. The water content *W/S*, defined as the ratio of the added water to the dry weight of the material, was determined according to a workability requirement (flow table value of about 170 mm [41]) for rendering mortars [42] as 0.18. The mechanical properties of the earth-based mortar were characterized according to EN 1015-11 [43]. After a drying period of 28 days under constant hygrothermal conditions (T= 20±2 °C and RH= 57.5±5%), three prismatic specimens with dimensions 40x40x160 mm^3 were tested under three-point bending and, afterwards, the remaining parts were tested under compression. The average flexural strength f_b was 0.5 MPa (CoV= 14%), while the average compressive strength f_c was 1.2 MPa (CoV= 12%). Finally, the Young's modulus E_m was evaluated by means of axial compression tests on three cylindrical specimens with 90 mm diameter and 175 mm height. The average Young's modulus E_m, computed by linear fitting of the stress-strain curves in the range 0-30% of f_c, was of about 4915 MPa (CoV= 20%).

As illustrated in Figure 1, the glass fibre mesh is woven and presents different properties according to the main orthogonal orientations. Therefore, the physical properties were assessed in both longitudinal *X* and transversal *Y* directions in terms of mesh size, linear density *TEX* [44], grammage *GSM* [45], density ρ and average cross-section of a single yarn A_y. The tensile behaviour of the dry mesh in the longitudinal direction was evaluated according to the procedure prescribed by ASTM D6637 [46] and RILEM TC-250 CSM [47]. According to Oliveira *et al.* [48], this direction presents the highest mechanical properties and, for sake of simplicity, it was the only direction considered in this experimental program. Thus, the mechanical behaviour was characterized

by testing five mesh specimens with width of 50 mm and free length of 300 mm. The average maximum linear force $P_{w,p}$ obtained was 18.4 kN/m (CoV 11%), while the average tensile strength f_t of a single yarn and the peak axial strain ε_{peak} were 626 MPa (CoV 11%) and 0.021 (CoV 10%), respectively. In addition, an average Young's modulus E_y of 32181 MPa (CoV 6%) was obtained by linear fitting of the tensile stress-strain curve in the range 0-30% of f_t. Table 1 summarizes the properties of both materials integrating the tested TRM solution.

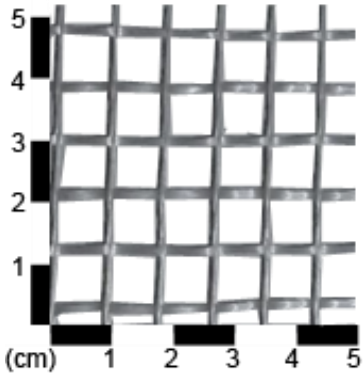

Figure 1. Glass fibre mesh integrating the tested TRM strengthening solution.

The pull-out specimens consisted of a glass fibre mesh band embedded in earth-based mortar cylinders with diameter of about 150 mm and height corresponding to the bonded length L_b. In the present study, only the specimens with bonded length 90 mm and 150 mm were considered. The specimens were casted ensuring the correct filling of the mould and perfect alignment of a single mesh band with 50 mm width, while the unbonded part of the mesh was kept vertically to avoid any damage due to bending. The drying period of the specimens was of 28 days under constant hygrothermal conditions (T= 20±2 °C and RH= 60±5 %), after which they were subjected to displacement controlled pull-out tests. The displacements of the mesh were recorded by means of one LVDT set at the free-end and two LVDTs set at the loaded-end close to the mortar surface (Figure 2).

Table 1. Properties of the earth-based mortar and glass fibre mesh used in the specimens of the pull-out tests.

Material	$P_{w,p}$ (kN/m)	ε_{peak} (mm/mm)	f_t (MPa)	E_y (MPa)	A_y (mm^2)	f_c (MPa)	f_b (MPa)	E_m (MPa)
Glass fibre mesh	18.42	0.021	625.8	32181	0.2944	-	-	-
Earth-based mortar	-	-	-	-	-	1.17	0.50	4915

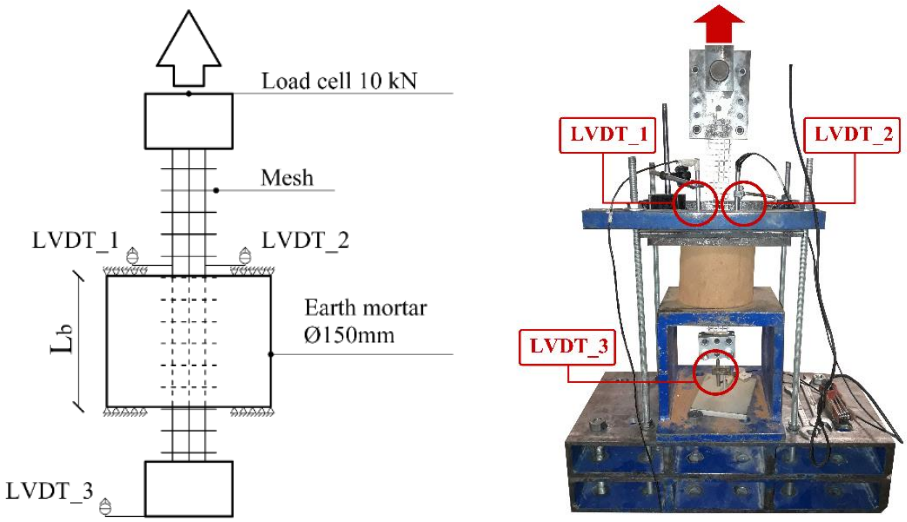

Figure 2. Setup of the pull-out tests.

The results are summarized in Table 2 in terms of elastic force per width $P_{el,w}$ and related elastic displacement at the loaded-end u_{el}, maximum force per width $P_{max,w}$ and ultimate displacement at the loaded-end u_{ult}. These values were subsequently considered in the algorithm to define the bond stress-slip relationship. It is reported that to identify the elastic force ($P_{el,w}$), linear regressions were performed increasing the value of the force and checking the goodness-of-fit. The end of the elastic response is considered when the goodness-of-fit decreases below a specific value or the slope of the fitting curve significantly changes. Figure 3a-d presents the response curves in terms of force per width, slip at the loaded-end and slip at the free-end for the two different bonded lengths considered. Based on the literature [32][36][38][39][49][50], the experimental pull-out curves can be divided into two zones, to which correspond different shear stress distribution along the mesh-mortar interface. A linear response is observed while the load is transmitted from the yarns to the matrix by adhesion and the shear strength is not achieved, which corresponds to the elastic force $P_{el,w}$. After this point, micro-cracks are developed at the interface, resulting in detachment between the two components and the response becomes nonlinear. During the nonlinear stage, adhesion is still in action at the interface of the bonded fibres, while friction between the fibres and the matrix is the resistant mechanism in the detached length. As the debonding propagates towards the free-end, the stiffness of the load-slip curve decreases, until the shear strength is attained at the free-end. In addition, as throughout reported in Romanazzi *et al.* [40], failure of the pull-out tests with bonded lengths of 50, 90 and 150 mm occurred in an embedded section of the yarns for tensile forces lower than the strength capacity of the dry mesh, as showed in Figure 4a and Figure 4b. This premature failure

of the mesh is attributed to damage accumulation in the yarns, caused by friction wearing between the earth-based mortar and the fibres as slipping progressed.

Table 2. Results of pull-out tests for the bonded lengths of 150 mm and 90 mm.

Specimen	L_b (mm)	$P_{el,w}$ (kN/m)	u_{el} (mm)	$P_{max,w}$ (kN/m)	u_{ult} (mm)
POGM150_1	150	2.64	0.1704	14.34	2.32
POGM150_2	150	2.48	0.2304	13.66	1.96
POGM150_3	150	2.92	0.1555	12.66	2.54
POGM150_4	150	2.38	0.1001	13.98	2.63
Average		2.61	0.1641	13.66	2.3625
(CoV %)		(9)	(33)	(5)	(13)
POGM90_1	90	3.13	0.2009	13.22	3.84
POGM90_2	90	2.99	0.1702	12.51	3.27
POGM90_3	90	2.83	0.1221	13.44	2.67
POGM90_4	90	2.67	0.0864	14.78	3.38
Average		2.91	0.1449	13.49	3.29
(CoV %)		(7)	(35)	(7)	(15)

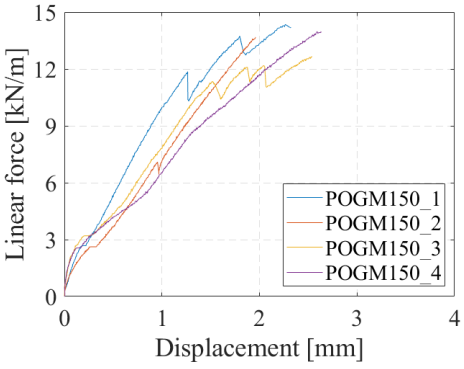

(a)

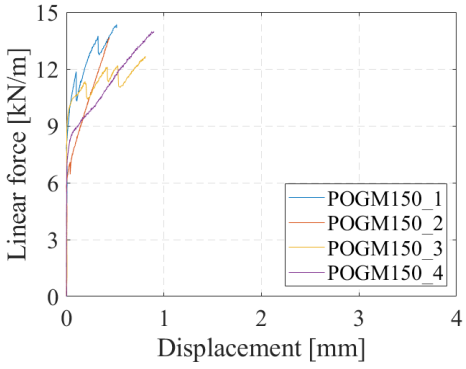

(b)

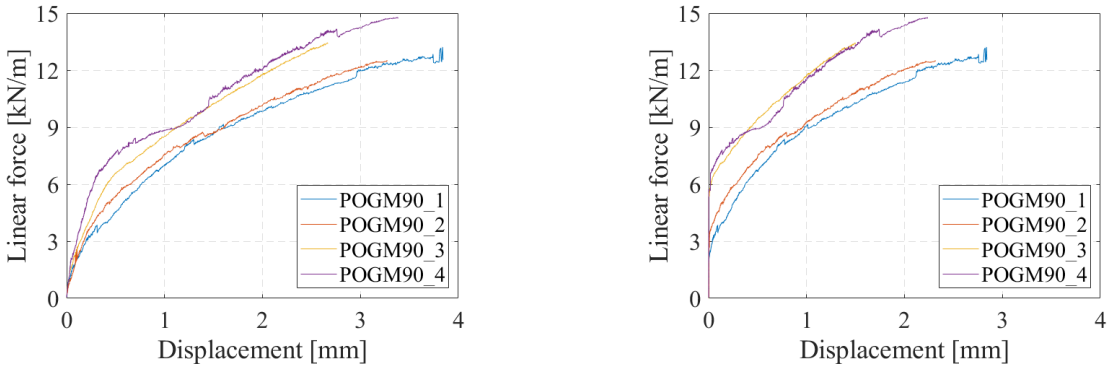

Figure 3. Pull-out experimental curves: a) loaded-end L_b 150 mm, b) free-end L_b 150 mm, c) loaded-end L_b 90 mm, and d) free-end L_b 90 mm.

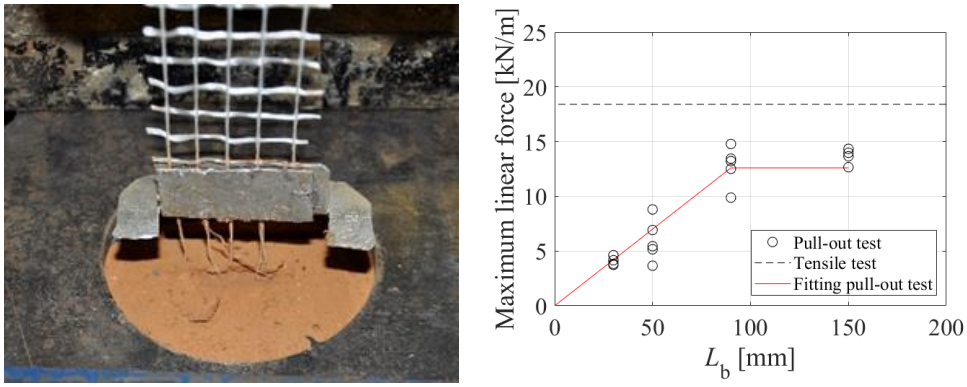

Figure 4. Experimental pull-out tests: a) damage of the fibres at embedded section; b) evolution of maximum linear force with bonded length and comparison with average tensile strength.

3. ANALYTICAL MODEL

Taking into account the results of the experimental program above-mentioned, the direct approach was adopted to process the experimental data of the pull-out tests and derive the corresponding analytical bond stress-slip law. Thus, an adhesion-friction constitutive law was assumed for the direct problem with a linear response up to the maximum shear strength τ_{max} and elastic slip s_{el}. Subsequently, the strength drops to the shear friction resistance τ_{fri}, which is constant until failure (see Figure 5)[51].

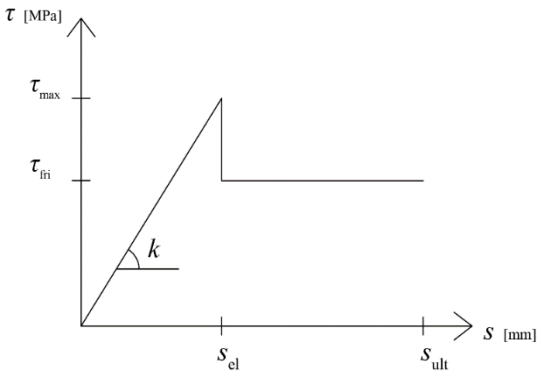

Figure 5. Adhesion-friction bond stress-slip relationship assumed to simulate the results of the pull-out tests.

Given the static equilibrium along the embedded length (see Figure 6), the tensile force in the yarn F is transferred to the matrix through the interface and then spread through the matrix to the reaction plate by compressive stress. Considering the infinitesimal interface length dx, the equilibrium can be expressed as:

$$\frac{dF}{dx} = p\tau(x) \qquad \textit{Eq. 1}$$

where p is the perimeter of the yarn and τ is the shear stress at the yarn-matrix interface.

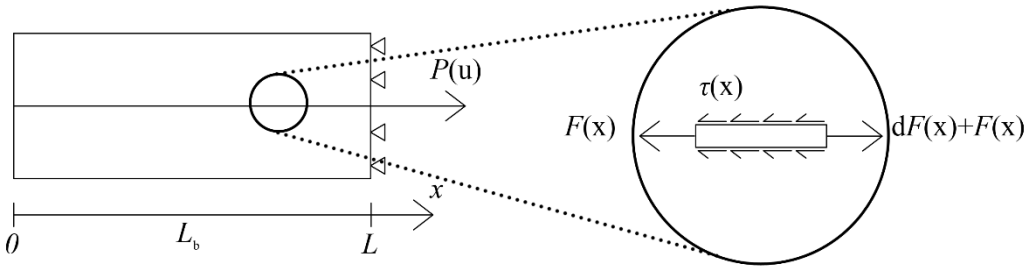

Figure 6. Static scheme of the interface during the pull-out test.

Since the axial elongation in the fibre and in the matrix can be defined, respectively, as $\varepsilon_{\mathrm{y}} = \frac{F}{A_{\mathrm{y}}E_{\mathrm{y}}}$ and $\varepsilon_{\mathrm{m}} = -\frac{F}{A_{\mathrm{m}}E_{\mathrm{m}}}$, the derivative of the displacement in the section x can be calculated as the difference between the elongation of the components $\frac{du}{dx} = \varepsilon_{\mathrm{y}} - \varepsilon_{\mathrm{m}}$, hence:

$$\frac{du}{dx} = \frac{F(x)}{A_{\mathrm{y}}E_{\mathrm{y}}} + \frac{F(x)}{A_{\mathrm{m}}E_{\mathrm{m}}} \qquad \textit{Eq. 2}$$

where A_{m}, A_{y}, E_{m} and E_{y} are the cross-sections and the Young's moduli of the matrix and fibre, respectively. It should be specified that the cross-section of the mortar A_{m} was not possible to be defined experimentally, therefore its value was assessed by mean of a sensitivity analysis of the presented approach. Substituting the Eq. 2 into Eq. 1, one obtains:

$$\frac{dF}{dx} = \frac{d^2u}{dx^2} = Qp\tau \quad \textit{Eq. 3}$$

where $Q = \frac{1}{A_y E_y} + \frac{1}{A_m E_m}$ is the relative axial stiffness between the two components. Eq. 3 represents the analytical problem statement of the pull-out test to be solved according to the stage in which the section is, as described herein.

3.1 Linear stage

During the adhesion phase, the assumed interface stress-slip relationship is linear with $\tau=\kappa u$ (Figure 5), which substituted in Eq. 3 leads to:

$$u'' - \lambda^2 u = 0 \quad \textit{Eq. 4}$$

with $\lambda = \sqrt{p\kappa Q}$. The general solution of this second order differential equation is:

$$u(x) = C_1 e^{\lambda x} + C_2 e^{-\lambda x} \quad \textit{Eq. 5}$$

which derived and substituted in Eq. 2 leads to:

$$F(x) = \frac{du}{dx}\frac{1}{Q} = \frac{1}{Q}\left(C_1 \lambda e^{\lambda x} - C_2 \lambda e^{-\lambda x}\right) \quad \textit{Eq. 6}$$

To solve Eq. 6 and obtain the constants C_1 and C_2, the boundary conditions are the force in the fibre at the free-end, which is null $F(0)=0$, while the force in the fibre at the loaded-end is equal to the pull-out force $F(L_b)=P$. Substituting the boundary conditions in Eq. 6, the coefficients C_1 and C_2 result $C_1 = C_2 = \frac{PQ}{\lambda\left(e^{\lambda L} - e^{-\lambda L}\right)}$. Therefore, replacing C_1 and C_2 in Eq. 6, the force distribution along the fibre $F(x)$ equals:

$$F(x) = P\frac{\left(e^{\lambda x} - e^{-\lambda x}\right)}{\left(e^{\lambda L_b} - e^{-\lambda L_b}\right)} = P\frac{sinh(\lambda x)}{sinh(\lambda L_b)} \quad \textit{Eq. 7}$$

while the shear $\tau(x)$ distribution along the interface is:

$$\tau(x) = \frac{dF}{dx}\frac{1}{p} = P\frac{\lambda}{p}\frac{cosh(\lambda x)}{sinh(\lambda L_b)} \quad \textit{Eq. 8}$$

The slip $s(x)$ distribution is calculated as the integral of the difference of the strains between the components up to coordinate (x) [32]:

$$s(x) = \int_0^x F(x)Q\,dx = PQ\frac{1}{sinh(\lambda L_b)}\int_0^x sinh(\lambda x)\,dx \quad \textit{Eq. 9}$$

For pull-out loads lower than the elastic limit load $F(L_b)=P<P_{el}$, the shear stress at the interface is less than the shear strength τ_{max} and the yarn and the matrix are fully bonded. Once the pull-out force achieves the elastic

load $F(L_b)=P=P_{el}$, the shear strength τ_{max} is attained in the loaded-end $x=L_b$ with the consequent debonding of that section. Hence, in such configuration the shear stress distribution is illustrated in Figure 7 and Eq. 8 becomes Eq. 10.

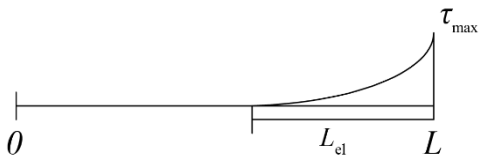

Figure 7. Shear stress distribution along the interface at the elastic load.

$$\tau(L_b) = \tau_{max} = P_{el}\frac{\lambda}{p}\frac{cosh(\lambda L)}{sinh(\lambda L)} \qquad \textit{Eq. 10}$$

While the slip at the loaded-end results:

$$s(L_b) = u_{el} = \int_0^{L_b} F(x)Q dx = PQ\frac{1}{sinh(\lambda L_b)}\int_0^{L_b} sinh(\lambda x)\,dx = P_{el}Q\frac{1}{sinh(\lambda L_b)}\frac{1}{\lambda}[cosh(\lambda L_b) - 1] \qquad \textit{Eq. 11}$$

Given the experimental elastic pull-out load and displacement (P_{el} and u_{el}, respectively), the shear strength τ_{max} and the shear stiffness of the interface κ are obtained by solving the system of equations composed of Eq. 10 and Eq. 11 at the coordinate of the loaded-end ($x=L_b$).

3.2 Nonlinear stage

With the loading going beyond the elastic limit $F(L_b)=P>P_{el}$, micro-cracks are developed at the interface and propagate in the further sections towards the free-end. Thus, the fibre and mortar are debonded in the length L_d, while they are still adhered in the remaining length L_b-L_d. In such configuration, the shear stress distribution is composed of constant frictional bond stress τ_{fri} in the debonding length $L_d<x<L_b$ and adhesion $\tau=\kappa u$ along the bonded length $L-(L_{el}-L_d)<x<L_b-L_d$, while the maximum shear strength τ_{fri} is achieved at the coordinate $x=L_b-L_d$ (see Figure 8).

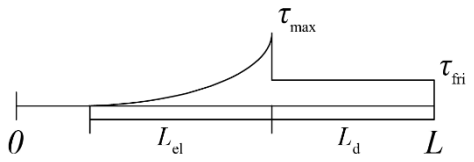

Figure 8. Shear stress distribution along the interface during the nonlinear response.

Therefore, the pull-out force is the sum of the forces resulting from adhesion and friction:

$$F(L_b) = P = F_{I_{max}} + F_{II} = \frac{\tau_{max}\, p}{\lambda} tanh[\lambda(L_b - L_d)] + \tau_{fri} p L_d \qquad \text{Eq. 12}$$

In this case, the boundary conditions are:

- $F(0)=0$
- $F(L_b - L_d) = \frac{\tau_{max}\, p}{\lambda} tanh[\lambda(L_b - L_d)]$
- $F(L_b)=P$

which can be used to solve Eq. 3, leading to the force distribution $F(x)$ at the elastic length:

$$F_I(x) = \frac{\tau_{max}\, p}{\lambda} tanh[\lambda(L_b - L_d)] \frac{sinh(\lambda x)}{sinh[\lambda(L_b - L_d)]} \qquad [L-(L_{el} - L_d) < x < L_b - L_d] \qquad \text{Eq. 13}$$

And at the debonded length:

$$F(x) = F_{I_{max}} + F_{II} = \frac{\tau_{max}\, p}{\lambda} tanh[\lambda(L_b - L_d)] + \tau_{fri} p (x - L_b + L_d) \qquad [L_b - L_d < x < L_b] \qquad \text{Eq. 14}$$

The slip along the yarn $s(x)$ can be evaluated as the sum of the slips according to the different stages in which the two parts of the yarns are, namely at the bonded section:

$$\begin{aligned} s_{el}(L_b - L_d) &= \int_0^{L_b - L_d} F_{I_{max}}(x) Q dx = \\ &= \int_0^{L_b - L_d} \tau_{max} \lambda Q\, p tanh[\lambda(L_b - L_d)] \frac{sinh(\lambda x)}{sinh[\lambda(L_b - L_d)]} dx = \\ &= F_{I_{max}} \lambda \frac{1}{sinh[\lambda(L_b - L_d)]} [cosh[\lambda(L_b - L_d)] - 1] \end{aligned} \qquad [L-(L_{el} - L_d) < x < L_b - L_d] \qquad \text{Eq. 15}$$

And at the debonded section:

$$\begin{aligned} s_{fri}(L_b) &= \int_{L_b - L_d}^{L_b} \frac{F(x)}{EA} dx = \\ &= \int_{L_b - L_d}^{L_b} F_{I_{max}} + \tau_{fri} p (x - L_b + L_d) Q dx = \\ &= L_d Q \left(F_{I_{max}} + \frac{\tau_{fri} p L_d}{2} \right) \end{aligned} \qquad [L_b - L_d < x < L_b] \qquad \text{Eq. 16}$$

Thus, the total slip equals:

$$s(L_b) = u = s_{el} + s_{fri} = F_{I_{max}} \lambda Q \frac{1}{sinh[\lambda(L_b - L_d)]} [cosh[\lambda(L_b - L_d)] - 1] + L_d Q \left(F_{I_{max}} + \frac{\tau_{fri} p L_d}{2} \right) \qquad \text{Eq. 17}$$

In this configuration, the unknowns are the debonded length L_d and the frictional bond stress τ_{fri}, which can be obtained by solving the system of equations composed of Eq. 12 and Eq. 17, considering as inputs the experimental pull-out force P and slip u in the nonlinear branch of the curve.

3.3 Damage model

As reported in Romanazzi *et al.* [40] and in section 2, damage due to friction between the components was observed in the experimental programme. In view of that, a simple damage model that considers the reduction of the effective cross-section of the yarn is here proposed as a function of the sliding.

The damage function can be defined as $\xi(u) = \frac{A_y - A_{y,d}}{A_y} x100$, where A_y and $A_{y,d}$ represent the initial cross-section area (undamaged state) and the reduced cross-section area of the yarn due to friction, respectively. Note that $A_{y,d}$ depends on the sliding undertaken by the yarn at the nonlinear stage. Thus, the ultimate load (P_{ult}) of the specimens from each bonded length can be considered to compute the damage at failure. In this case, the reduced cross-section is evaluated as $A_{y,d} = \frac{P_{ult}}{n^{\circ} f_t}$, where f_t is the tensile strength of the dry mesh and n is the number of yarns. In this framework, a correlation between the value of the damage and the sliding of the nonlinear stage (u-u_{el}) was found, which is further expressed in Eq.18. In addition, the constraint $\xi(0) = 0$ was introduced, meaning that the damage is null at the end of the elastic stage ($u = u_{el}$).

$$\xi(u) = \left(1.541e^{1.294(u-u_{el})} - 1.541\right) X \frac{1}{100} \qquad \textit{Eq. 18}$$

The difference between the ultimate slip u_{ult} and the elastic slip u_{el} represents the sliding for which the damage involves a reduced section of the yarn, leading to an apparent tensile strength lower than the tensile strength of the dry mesh. Therefore, the value of $\xi(u) = \left(1.541e^{1.294(u-u_{el})} - 1.541\right) X \frac{1}{100}$ (see Figure 9) is introduced as a factor to reduce the cross-section of the yarn in evaluation of the friction force $\tau_{fri} p\left(\xi(u)\right) L_d$, which is then considered in the system of equations of the nonlinear stage, composed of Eq. 12 and Eq. 17.

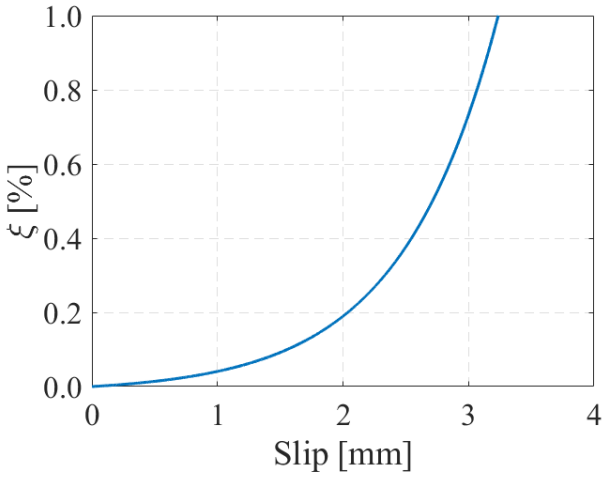

Figure 9. Damage curve of the section of the yarn due to slip.

4. IMPLEMENTATION AND RESULTS

The algorithm to solve the problem stated in Section 3 for the different stages is described in this section and implemented for each pull-out specimen tested in the experimental program. After individuating the end of the linear stage, the corresponding pull-out force P_{el} and displacement u_{el} were considered to solve the system of equations Eq. 10 and Eq. 11. Therefore, the maximum shear stress τ_{max} and the shear stiffness κ were evaluated. To verify the reliability of the elastic values, a linear regression of the pull-out values up to P_{el} and u_{el} can be performed and the R^2 value checked. During the nonlinear stage, several pairs of pull-out force-displacement P-u can be considered to solve the system of equations constituted by Eq. 12 and Eq. 17 for obtaining the debonded length L_d and the frictional bond stress τ_{fri}. For this reason, the experimental curves were discretized by considering load points in increments of 10% of P_{max} and the corresponding displacement u. For each step, the damage function $\xi(u)$ was calculated according to Eq. 18 and the damage was considered through $\tau_{fri}p(\xi(u))L_d$ in the system of equations constituted by Eq. 12 and Eq. 17. Since different values of shear friction τ_{fri} resulted from each step, the average value of τ_{fri} was calculated as to be lower than or equal to the shear strength τ_{max}. In the cases of such restriction being unverified, the shear friction is considered equal to the shear strength.

Finally, the obtained bond stress-slip law was verified through the simulation of the pull-out experiments, which was performed by increasing the value of the relative displacement at the loaded-end $u(L_b)$, while the corresponding value of pull-out force was evaluated from Eq. 10. When the displacement at the loaded-end was equal to the elastic slip $u(L_b)=s_{el}$, the end of the linear behaviour was achieved. Further increasing of the displacement makes the response become nonlinear. Thus, the corresponding pull-out force was calculated by solving the system of equations constituted by Eq. 12 and Eq. 17, where the unknowns are the pull-out force P and the debonding length L_d. At this stage, the damage model by Eq. 18 was introduced in Eq. 12, while the failure of the mesh was controlled for each step of pull-out force by checking if the corresponding tensile stress in the yarn was lower than the tensile strength of the dry mesh, as in (Eq. 19):

$$\sigma_y(P(u)) = \frac{P}{A_y(1-\xi(u))} \qquad \textit{Eq. 19}$$

When this last condition was not verified, the tensile failure of the mesh was achieved and the simulation stopped. Therefore, the simulated pull-out force-slip curve was obtained and compared with the experimental

curve to verify the accuracy. Afterwards, a sensitivity analysis was performed by varying the values of τ_{max} and s_{el} in about -10% and +10%, leading to a set of 9 constitutive laws for each sample, which were further checked by simulation of the pull-out response as previously described. Since the bond stress-slip law is independent from the geometry of the specimen, the optimum values of τ_{max} - s_{el} were selected among all the 9 possibilities and were used to verify the simulations of the different bonded lengths.

The methodology described above was implemented considering the experimental values reported in Table 2, which allowed to obtain the BSRs of each specimen, as summarized in Table 3. It should be noted that the proposed analytical model intends to simulate the response of pull-out tests in which damage due to friction between fibres and matrix influences the failure mode. Accordingly, a reducing factor ($\xi(u)$) for the geometrical properties of the composite is introduced, which in this case is referred to the cross-section of the yarn, according to what was observed in the experimental programme. Thereby, the experimental observations could be reproduced. It is also specified that, while the approach of considering a reducing factor in case of damage due to friction can be generally applied, the inferred model may require calibration for geometries different from the ones considered in the present investigation.

As anticipated, τ_{fri} must not exceed the shear strength τ_{max}, differently the value of the shear friction is assumed as the shear strength. As reported in Table 3, such condition was not satisfied in all the cases. A scattering in the results can be observed, in particular for the values of the interface stiffness κ, which present a coefficient of variation of 61%. Such dispersion can be due to the considered experimental elastic displacement s_{el}.

Table 3. Bond stress-slip parameters obtained by implementation of the direct problem approach.

Simulation	τ_{max} (MPa)	s_{el} (mm)	κ	τ_{fri} (MPa)	s_{ult} (mm)
POGM150_1	0.398	0.1704	2.336	0.398	2.6100
POGM150_2	0.235	0.2304	1.022	0.235	3.0800
POGM150_3	0.567	0.1316	4.305	0.567	2.2000
POGM150_4	0.593	0.0906	6.540	0.593	2.1400
POGM90_1	0.392	0.2009	1.951	0.392	2.6800
POGM90_2	0.459	0.1702	2.697	0.459	2.4800
POGM90_3	0.672	0.3066	2.191	0.672	2.1000
POGM90_4*	1.220	0.2207	5.527	1.220	3.65

Average	0.47	0.1858	3.006	0.47	2.4700
(CoV %)	(31%)	(38%)	(61%)	(31%)	(14%)

* The results obtained for POGM90_4 are considered as outliers [52].

Subsequently, the sensitivity analysis was performed and the optimized parameters were assessed from the 9 combinations of ($\tau_{max} - s_{el}$) for each specimen, which led to the bond-slip laws presented in Figure 10 and Table 4. It should be noted that the shear strength τ_{max}, the elastic slip s_{el}, the elastic stiffness κ and the frictional bond stress τ_{fri} are equal for both bonded lengths (90 mm and 150 mm), while the ultimate slip s_{ult} may vary, since it is affected by the damage of the yarn.

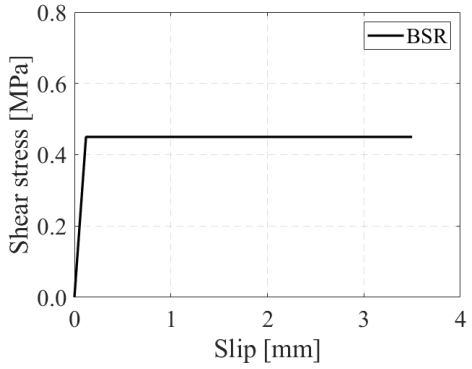

Figure 10. Sensitivity analysis of the BSR parameters.

Table 4. Optimized bond stress-slip parameters resulting from the sensitivity analysis.

Simulation	τ_{max} (MPa)	s_{el} (mm)	κ	τ_{fri} (MPa)	s_{ult} (mm)
POGM150	0.45	0.12	3.75	0.45	2.45
POGM90					2.47

Finally, considering the parameters reported in Table 4, the simulation of the pull-out tests was performed for the bonded lengths of 150 mm and 90 mm. The comparison of the simulated and experimental curves *P(u)* at the free-end and loaded-end is presented in Figure 11. Although differences in the fitting of the analytical solution with the experimental data can be observed, the proposed algorithm reproduces well the elastic response and the nonlinear behaviour of the pull-out tests. Such differences can be ascribed to the fact that the pull-out specimens consisted of a mesh band embedded in earth-based mortar, therefore uneven transmission of loads along the width of the mesh can occur during the test. Table 5 compares the average values of the parameters obtained from the experimental curves with the values obtained from the simulated curves, namely

in terms of elastic force per width $P_{el,w}$, elastic slip u_{el}, maximum force per width $P_{max,w}$, ultimate slip u_{ult}, force per width at the sliding onset $P_{sl,w}$ and ultimate slip at the free-end $u_{sl,ul}$. Although all the values obtained from the analytical model are within the range of variation of the observations, their difference can be better observed when the percentage error of the simulation is calculated with respect to the experimental values (see Table 6). The elastic pair $P_{el,w} - u_{el}$ and the maximum force per width $P_{max,w}$ are well predicted as the error is relatively small with respect to the experimental scattering. In the case of the ultimate displacement u_{ult} and force at the sliding onset $P_{sl,w}$, the predicted values agree with those obtained experimentally for the specimens with bonded length of 150 m, while underestimate the experimental values for the specimens with bonded length of 90 mm. Despite that, the values are within the limits of the scattering from the experimental results. As for the ultimate slip at the free-end $u_{sl,ul}$, the value calculated from the analytical model for the bonded length of 90 mm meets the experimental one, although it is overestimated for the bonded length of 150 mm.

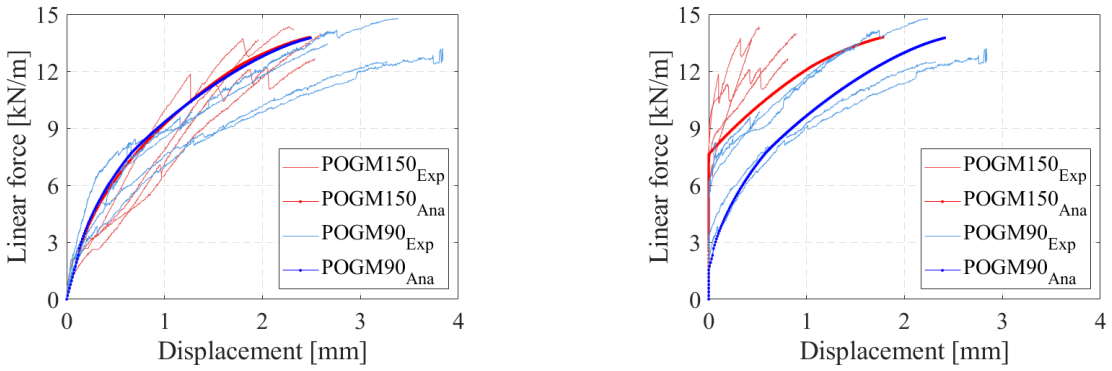

Figure 11. Simulation of the pull-out tests and comparison with the experimental curves, considering the slip at the: (a) loaded-end and (b) free-end.

Table 5. Comparison of the parameters obtained from the experimental curves with those obtained from the analytical curves (CoV in between brackets).

L_b	$P_{el,w}$		u_{el}		$P_{max,w}$		u_{ult}		$P_{sl,w}$		$u_{sl,ul}$	
(mm)	(kN/m)		(mm)		(kN/m)		(mm)		(kN/m)		(mm)	
	Exp	Ana	Exp	Ana	Exp	Ana	Exp	Ana	Exp	Ana	Exp	Ana
150	2.76 (9%)	2.32	0.1545 (32%)	0.1200	13.66 (5%)	13.68	2.36 (13%)	2.50	7.87 (17%)	7.67	0.6655 (33%)	1.78
90					13.49	13.56	3.29	2.52	4.64	1.35	2.2241	2.44

(7%)	(15%)	(37%)	(25%)	

Table 6. Errors of the simulated parameters with respect to the experimental ones.

L_b (mm)	$P_{el,w}$ (%)	u_{el} (%)	$P_{max,w}$ (%)	u_{ult} (%)	$P_{sl,w}$ (%)	$u_{sl,ul}$ (%)
150	16.94	22.33	-0.15	-5.93	2.54	-167.47
90			-0.52	23.40	70.91	-9.71

5. CONCLUSIONS

A bond stress-slip analytical model of a TRM-based solution for strengthening rammed earth dwellings is here calibrated based on an experimental program conducted by the authors. Firstly, the material properties of the composite solution and the results of previous pull-out tests are presented. In this regard, the experimental curves of the pull-out tests evidenced an initial linear response, in which the load is transferred through the interface solely by adhesion. After this stage, the response became nonlinear due to achievement of the shear strength, which implicates the formation of micro-cracks at the interface and leads friction to be the bond mechanism of the debonded components. Therefore, the direct boundary problem approach is adopted, and an adhesion-friction bond stress-slip law was hypothesized.

In addition, a novel damage model was inferred to reduce the effective area of the fibers, as an empirical correlation between the level of sliding and the loss of strength capacity with respect to the dry mesh was experimentally observed.

In conclusion, the proposed analytical model reproduces well the elastic and nonlinear response of the pull-out tests, as the maximum force per width, the elastic force per width and the corresponding elastic slip obtained by the model are similar to the experimental values. Nevertheless, the ultimate slip at the loaded-end is underestimated for the bonded length of 90 mm, while the ultimate slip at the free-end is overestimated for the bonded length of 150 mm. Despite that, the analytical values were found to be within the range of scattering of the experimental results. Therefore, the proposed analytical model adequately simulates the interface matrix-

fibres behaviour of the TRM strengthening under study and might be implemented in further numerical and analytical applications.

6. ACKNOWLEDGMENTS

This work was partly financed by FEDER funds through the Operational Programme Competitiveness Factors (COMPETE 2020) and by national funds through the Foundation for Science and Technology (FCT) within the scope of project SafEarth - PTDC/ECM-EST/2777/2014 (POCI-01-0145-FEDER-016737). The support from grant SFRH/BD/131006/2017 is also acknowledged.

7. REFERENCES

[1] Houben H., Guillaud H. (2008) Earth construction: a comprehensive guide. London, Intermediate Technology Publication.

[2] Silva R.A., Oliveira D.V., Miranda T., Cristelo N., Escobar M.C., Soares E. (2013) Rammed earth construction with granitic residual soils: The case study of northern Portugal. Construction and Building Materials, 47, 181-191.

[3] Minke G. (2006) Building with earth, design and technology of a sustainable architecture. Basel- Berlin-Boston, Birkhäuser Architecture.

[4] Jaquim P.A., Augarde C.E., Gerrard C.M. (2008) A chronological description of the spatial development of rammed earth techniques. International Journal of Architectural Heritage, 2, 377-400.

[5] Fernandes M. (2013) A Taipa no mundo. (C.d. Porto, Ed.) DigitAR, 1, 14-21.

[6] Silva R.A., Mendes N., Oliveira D.V., Romanazzi A., Domínguez-Martínez O., Miranda, T. (2018) Evaluating the seismic behaviour of rammed earth buildings from Portugal: from simple tools to advanced approaches. Engineering Structures, 157, 144-156.

[7] Correia M. (2007) Rammed earth in Alentejo. Lisbon, Argumentum.

[8] Lourenço P.B., Torrealva D., Cancino C., Wong K., Karanikoloudis G. and Ciocci, M.P. (2017) Innovative traditional technologies for rehabilitation and protection of earthen structures: the Getty Conservation Institute seismic retrofitting project. In proc. of PROHITEC17 3rd International Conference on Protection of Historical Constructions, Lisbon.

[9] Costa A.A., Varum H., Rodrigues H., Vasconcelos G. (2015) Seismic behaviour analysis and retrofitting of a row building. In Correia M., Lourenço P.B., Varum H., Seismic Retrofitting: Learning from vernacular architecture. London, Taylor and Francis Group.

[10] De Felice G., De Santis S., Garmendia L., Ghiassi B., Larringa P., Lourenço P.B., Oliveira D.V., Paolacci F., Papanicolaou C.G. (2014) Mortar-based systems for externally bonded strengthening of masonry. Materials and Structures, 47, 2021-2037.

[11] Ghiassi B., Marcari G., Oliveira D.V., Lourenço P.B. (2012) Numerical analysis of bond behavior between masonry bricks and composite materials. Engineering Structures, 43, 210- 220.

[12] Valluzzi M.R., Modena C., De Felice G. (2014) Current practice and open issues in strengthening historical buildings with composites. Materials and Structures, 47, 1971-1985.

[13] Righetti L., Edmondson V., Corradi M., Borri A. (2016) Fiberglass grids as sustainable reinforcement of historic masonry. Materials, 9, 1-17.

[14] Noguez R., Navarro S. (2005) Reparación de muros de adobe con el uso de mallas sintéticas. In proc. of International Conference SismoAdobe 2005: architecture, construction and conservation of earthen buildings in seismic areas, Lima.

[15] Yamin L., Phillips C., Reyes J., Rivero S., Ruiz D. (2007) Estudios de vulnerabilidad sísmica, rehabilitación y refuerzo de casas en adobe y tapia pisada. Apuntes: Revista de estudios sobre património – Journal of Cultural Heritage Studies, 20, 286-303.

[16] Zavala C., Igarashi L. (2005) Propuesta de Reforzamiento para Muros de Adobe. In proc. of International Conference SismoAdobe 2005: architecture, construction and conservation of earthen buildings in seismic areas, Lima.

[17] Vargas J., Blondet M., Ginocchio F., García G. (2005) 35 Años de investigaciones en sismo adobe: la tierra armada, International Conference SismoAdobe 2005: architecture, construction and conservation of earthen buildings in seismic areas, Lima.

[18] Blondet M., Torrealva D., Vargas J., Velasquez J., Tarque N. (2006). Seismic Reinforcement of Adobe Houses Using External Polymer Mesh. In proc. of First European Conference on Earthquake Engineering and Seismology, Geneva.

[19] Michiels T.L.G. (2014) Seismic retrofitting techniques for historic adobe buildings. International Journal of Architectural Heritage, 9, 1059-1068.

[20] Torrealva D. (2016). Static and dynamic testing for validating the polymer grid as external reinforcement in earthen buildings. In proc. of Brick and Block Masonry: Proceedings of the 16th International Brick and Block Masonry Conference, Padova.

[21] Figueiredo A., Varum H., Costa A., Silveira D., Oliveira C. (2013) Seismic retrofitting solution of an adobe masonry wall. Materials and Structures, 46, 203-219.

[22] Wang Y., Wang M., Liu K., Pan W., Yang X. (2017) Shaking table tests on seismic retrofitting of rammed earth structures. Bulletin of Earthquake Engineering, 3, 1037-155.

[23] Fagone M., Loccarini F., Ranocchiai G. (2017) Strength evaluation of jute fabric for the reinforcement of rammed earth structures. Composites Part B: Engineering, 133, 1-13.

[24] Van Balen K., Papayianni I., Van Hees R., Binda L., Waldum A. (2005). Introduction to requirements for and functions and properties of repair mortars. RILEM TC 167-COM: 'Characterisation of old mortars with respect to their repair'. Materials and Structures, 3, :781–85.

[25] Dalalbashi A., Ghiassi B., Oliverira D.V. and Freitas A. (2018) Effect of test setup on the fiber-to-mortar pull-out response in TRM composites: experimental and analytical modeling. Composites: Part B, 143, 250-268.

[26] D'Ambrisi A., Feo L. and Focacci F. (2013) Experimental analysis on bond between PBO-FRCM strengthening materials and concrete. Composites: Part B, 44, 524-532.

[27] Donnini J., Lancioni G. and Corinaldesi V. (2018) Failure modes in FRCM systems with dry and pre-impregnated carbon yarns: experiments and modeling. Composites: Part B, 140, 57-67.

[28] Soranakom C. and Mobasher B. (2009) Geometrical and mechanical aspects of fabric bonding and pullout in cement composites. Materials and Structures, 42, 765-777.

[29] Li Y., Bielak J., Hegger J. and Chudoba R. (2018) An incremental inverse analysis procedure for identification of bond-slip laws in composites applied to textile reinforced concrete. Composites: Part B, 137, 111-122.

[30] Banholzer B., Brameshuber W. and Jung W. (2005) Analytical simulation of pull-out tests: the direct problem. Cement and concrete composites, 27, 93-101.

[31] Oliveira D.V., Basilio I. and Lourenço P.B. (2011) Experimental bond behavior of FRP sheets glued on brick masonry. Journal of composites for construction, 1, 32-41.

[32] Sueki S., Soranalom C., Mobasher B., Member ASCE and Peled A. (2007) Pullout-slip response of fabrics embedded in a cement paste matrix. Journal of materials in civil engineering, 19, 718-727.

[33] Banholzer B., Brameshuber W. and Jung W. (2006) Analytical simulation of pull-out tests: the inverse problem. Cement e concrete composites, 28, 564-571.

[34] Banholzer B. (2006) Bond of a strand in a cementitious matrix. Materials and structures, 39, 1015-1028.

[35] Naaman A.E., Member ASCE, Namur G.G., Alwan J.M. and Najm H.S. (1991) Fiber pullout and bond slip. I: analytical study. Journal of structural engineering, 117, 2769-2790.

[36] Carozzi F.G., Colombi P., Fava G. and Poggi C. (2016) A cohesive interface crack model for the matrix–textile debonding in FRCM composites. Composite structures, 143, 230-241.

[37] Ferreira S.R., Martinelli E., Pepe M., Silva F.D. and Filo R.D.T. (2016) Inverse identification of the bond behavior for jute fibers in cementitious matrix. Compistes: Part B, 95, 440-452.

[38] D'Antino T., Colombi P., Carloni C. and Sneed L.H. (2018) Estimation of a matrix-fiber interface cohesive material law in FRCM-concrete joints. Composite structures, 193, 103-112.

[39] Focacci F., D'Antino T., Carloni C., Sneed L.H. and Pellegrino C. (2017) An indirect method to calibrate the interfacial cohesive material law for FRCM-concrete joints. Materials and design, 128, 206-217.

[40] Romanazzi A., Oliveira D.V. and Silva R.A. (2019) Experimental investigation on the bond behavior of a compatible TRM-based solution for rammed earth heritage. International Journal of Architectural Heritage, DOI: 10.1080/15583058.2019.1619881.

[41] BS EN 1015 (1999) Methods of test for mortar for masonry. Part 3: determination of consistence of fresh mortar (by flow table)

[42] Gomes M.I., Faria P., Gonçalves T.D. (2013) The compatibility of earth-based repair mortars with rammed earth substrates. In proc. of 3rd Historic Mortars Conference, Glasgow.

[43] BS EN 1015 (1999) Methods of test for mortar for masonry. Part:11 determination of flexural and compressive strength of hardened mortar.

[44] Vasconcelos R. M. (1993). Contribuição à aplicação de técnicas de inteligência artificial na tecnologia da fiação. PhD thesis, Universidade do Minho, Guimarães.

[45] ISO 3374 (2000) Reinforcement products. Mats and fabrics. Determination of mass per unit area.

[46] ASTM D6637 (2015) Standard test method for determining tensile properties of geogrids by the single or multi-rib tensile method.

[47] De Felice G., Aiello M.A., Caggegi C., Ceroni F., De Santis S., Garbin E., Gattesco N., Hojdys L., Krajewski P., Kwiecień A., Leone M., Lignola G.P., Mazzotti C., Oliveira D., Papanicolaou C., Poggi C., Triantafillou T., Valluzzi M.R., Viskovic A. (2018) Recommendation of RILEM Technical Committee 250-CSM: Test method for Textile Reinforced Mortar to substrate bond characterization . Materials and Structures, 51, 95.

[48] Oliveira D.V., Silva R.A., Barroso C., Lourenço P.B. (2018) Characterization of a compatible low cost strengthening solution based on the TRM Technique for Rammed Earth. Key Engineering Materials, 747, 150-157.

[49] Zhang X.B., Aljewifi H. and Li J. (2013) Failure behaviour investigation of continuous yarn reinforced cementitious composites. Construction and building materials, 47, 456-464.

[50] D'Antino T., Carloni C., Sneed L.H. and Pellegrino C. (2014) Matrix-fiber bond behavior in PBO FRCM composites: a fracture mechanics approach. Engineering fracture mechanics, 117, 94-111.

[51] Colombi P., D'Antino T. (2019) Analytical assessment of the stress-transfer mechanism in FRCM composites. Composite Structures, 220, 961-970.

[52] ASTM E178 (2002) Standard practice for dealing with outlying observations.